ACS OMEGA

http://pubs.acs.org/journal/acsodf

Article

Understanding Complex Electron Radiolysis in Saline Solution by Big Data Analysis

Zhihao Zhang,[‖] Hongxuan Guo,*[,‖] Bo Liu, Dali Xian, Xuanxuan Liu, Bo Da, and Litao Sun*

Cite This: *ACS Omega* 2022, 7, 15113−15122

Read Online

ACCESS | Metrics & More | Article Recommendations | Supporting Information

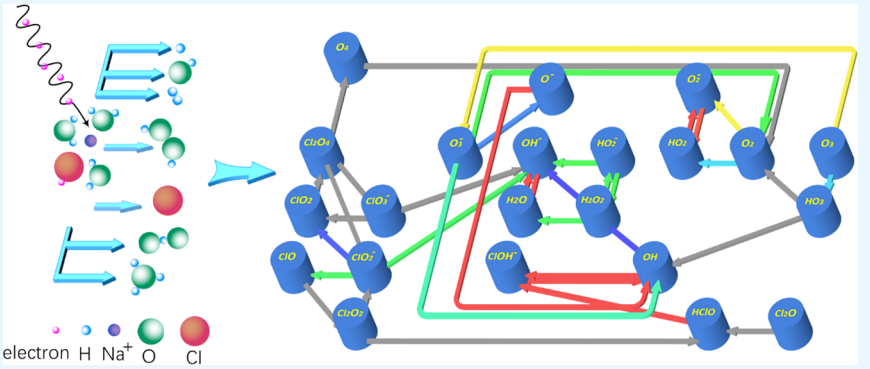

ABSTRACT: In this article, we developed a new method to analyze the complex chemical reactions induced by electron beam radiolysis based on big data analysis. At first, we built an element transport network to show the chemical reactions. Furthermore, the linearity between the species was quantified by Pearson correlation coefficient analysis. Based on the analysis, the mechanism of the high linearity between the special species pairs was interpreted by the element transport roadmap and chemical equations. The time variation of the pH of the solution and bubble formation in the solution were analyzed by simulation and data analysis. The simulation indicates that O_2 and H_2 can easily oversaturate and form bubbles. Finally, the radiolysis of high-energy electrons in pure water was analyzed as a reference for the radiolysis of high-energy electrons in saline solution. This work provides a new method for investigating a high-energy electron radiolysis process and for simplifying a complex chemical reaction based on quantitative analysis of the species variation in the reaction.

INTRODUCTION

Radiolysis is a complicated phenomenon induced by ion beams, electron beams, and other radioactive particles on condensed materials. It is important to analyze the radiolysis of an aqueous solution, such as saline, in various applications. For instance, the efficiency of radiotherapy is dominated by the radiolysis of the external radioactive beam, radiotherapy implants, and injections on tumors and living cells.[1,2] Living cells exposed to beta rays and other radioactive sources are damaged by direct radiation hazards and radiation chemical reactions.[3−11] In addition to health science, radiolysis has been investigated in other fields. In radioactive waste disposal work, the service life of metal containers for high-radioactivity liquid storage is reduced because the corrosion of the metals is accelerated by the products of water radiolysis. In some chemical experiments, radiolysis products actuate the experiments for nanoparticle formation and evolution.[12−15] Nanostructures printed by electron beams are also controlled by free radicals induced by the radiolysis of high-energy electrons in water and other solutions.[13,16−22] Thus, the exploration of radiolysis is important and instructive to engineering and technologies.

Multiple water radiolysis product yield rates by pulsed electron beams have been measured since 1962.[23,24] Le Caër defined the water radiolysis process into three stages.[25] In the first stage, water molecules undergo relaxation processes after energy is deposited and provide excited molecules, ionized molecules, and subexcitation electrons. In the second stage, molecules undergo complex physical reactions such as ion−molecule reactions and dissociative relaxation. In the last stage, species undergo chemical reactions and diffuse in water. Schneider revealed the relationship between the water radiolysis product concentration and electron beam setting data by mathematical models and experiments.[26]

Based on the radiolysis of water, the relationship between the yield rate of the radiolysis products and the concentration

Received: February 19, 2022
Accepted: April 8, 2022
Published: April 21, 2022

of the aqueous saline solution was investigated.[27−32] Molecular decomposition and chemical reactions are used to explain the complex species generated during radiolysis. Energy absorption-induced molecular decomposition in solution yields free radicals and other species. Chemical reactions rebuild species chemical bonds and produce other species. These complex species irreversibly change solutions. This complex process is difficult to understand through the related more than one hundred chemical equations. Normal saline is a basic component of human cells, and normal saline radiolysis process research is important to understand radioactive damage to cells. Thus, we analyzed the radiolysis of high-energy electrons in normal saline solution by a big data method. The chemical reaction induced by radiolysis was clarified based on big data analysis.

MODEL DEVELOPMENT

Kinetic Model. A kinetic model of the radiolysis process was established based on the chemical reactions in normal saline solution. In this model, we analyzed the formation of species and the chemical reaction among them. According to Le Caër's three-stage theory, the radiolysis process can be divided into three stages. However, the theory of how the electron beams affect water during the radiolysis process has great development.[33] In Taylor's words, the radiolysis effect is the reactions by free radicals produced by water and electron. Thus, the radiolysis process can be grouped into two stages by varied features in the species transformation. In the first stage, the electron beam transmits energy to the water molecules and yields free radicals. This process stops with the removal of the electron beam. In the first stage, new species yielded by the electron beam are listed in eqs 1 and 2. In eq 1, the species yield hydrogen and oxygen atoms with new bonds. Moreover, in eq 2, chloride ions become chloride atoms with electrons lost, and sodium ions are always stable. In radiation dosimetry, the G value is used to define the rate of the new species' yield or disappearance in the radiolysis process. In the second stage, all species react with others based on the chemical equations shown in the SI (Supporting Information).

$$H_2O{\cdot}e_h^-,\ H^{\cdot},\ OH^{\cdot},\ H_2,\ H_2O_2,\ H_3O^+,\ HO_2^{\cdot} \tag{1}$$

$$Cl^-{\cdot}e_h^-,\ Cl \tag{2}$$

The temporal evolution of the species induced by electron beam irradiation was analyzed in this paper; thus, we assumed that the cross area of the solution was exposed homogeneously. A simplified kinetic model was established to describe the temporal evolution of the species concentrations.[26] In addition, the mass of the analyzed solution is a constant in the model. It is suggested that the heat effect induced by laser pulse irradiation increases the temperature of the sample by more than 10 °C.[34] We find that the dose rate in Liu's work[34] is about 2.5×10^7(Gy/S), this dose rate is the same as the electron beam with 300 keV voltage and 350 pA current. However, living cell research will not use such huge dose rates; on the one hand, the high current will kill the living cell quickly while, on the other hand, the high voltage cannot provide image information clearly. The settings of dose rate in living cell research[35,36] usually are under 2.5×10^6(Gy/s); thus, the heat effect is limited and it can be ignored in this model. The diffusion calculation was neglected because space influence was excluded from consideration in this paper.

The concentration variation rate of all species in the saline solution was calculated by eq 3 with an improved Euler method, where R_i was calculated by eq 4, the dose rate of radiolysis was 7.5×10^7 (Gy/s), and the G values of the radiolysis are listed in Table 1. The detailed symbol description is listed in Table 3. In this work, we calculated the species concentration with time from 0 to 0.1 s with a step of 10^{-10} s; thus, we had 10^9 data points for each species.

Table 1. G Value for Nine Species

name	G value (100 eV)
e_h^-	3.58
H_3O^+	4.09
OH^-	0.95
H_2O_2	2.83
$H^{\cdot}$	1
$OH^{\cdot}$	3.32
$HO_2^{\cdot}$	0.08
H_2	0.27
Cl	0.6175

$$\frac{\partial C_i}{\partial t} = -\sum_i r_{i,j}C_iC_j + \sum_{l,k\neq i} r_{l,k}C_lC_k + R_i \tag{3}$$

$$R_i = \frac{\rho\psi G_i}{F}(M/s) \tag{4}$$

Pearson Correlation Coefficient (PCC) Calculation. PCC analysis is an effective method for displaying two database relationships in machine learning technique studies.[37] In this paper, the linearity of the concentration of the species was indicated by the Pearson correlation coefficient (PCC). After that, highly correlated species pairs were set according to linearity. In this work, the PCC of species was calculated with eqs 5−7. We chose 1.1×10^5 data points from 10^9 data points. The data picking rule was as follows: the complete data from 10^{-10} to 10^{-5} s were chosen; one data point for each 10^{-5} s from 10^{-5} to 10^{-1} s was chosen. We performed logarithmic calculations for previously selected data in the PCC calculation.

$$Pcc_{l,i} = \frac{A}{B} \tag{5}$$

$$A = n\sum_{v=1}^{n} C_{l,v}C_{i,v} - n\sum_{v=1}^{n} C_{l,v}\sum_{t=1}^{n} C_{i,v} \tag{6}$$

$$B = \sqrt{n\sum_{v=1}^{n} C_{l,v}^2 - \left(\sum_{v=1}^{n} C_{l,v}\right)^2} \cdot \sqrt{n\sum_{v=1}^{n} C_{i,v}^2 - \left(\sum_{v=1}^{n} C_{i,v}\right)^2} \tag{7}$$

Normalized Conventional Rate Calculation. In eq 8, variable $V_{ie}(t)$ is the conventional rate, which stands for the transform rate from original species i to product e. $r_{i,j}$ is the rate constant in the chemical reaction about species i and j to yield species e. C_i and C_j is the concentration of species i and j, respectively. In eq 9, variable $P_{ie}(t)$ is the normalized conventional rate, which stands for the form percent for species e, x in variable $V_{ix}(t)$ is the species that can be yielded by species i, for instance, species O_3 can yield O_2, HO_2, and O_3^-; thus, x stands for O_2, HO_2, and O_3^-. Species transform path effect can be qualified by $P_{ie}(t)$: high $P_{ie}(t)$ means species i

https://doi.org/10.1021/acsomega.2c01010
ACS Omega 2022, 7, 15113−15122

transformation to e with high percent while low $P_{ie}(t)$ means species i transformation to e with low percent.

$$V_{ie}(t) = \sum r_{i,j} C_i C_j \quad (8)$$

$$P_{ie}(t) = \frac{V_{ie}(t)}{\Sigma V_{ix}(t)} \quad (9)$$

C_i and C_j are functions of time; thus, $P_{ie}(t)$ is dependent on time. According to $P_{ie}(t)$ development, transform paths can be classified into three groups as Table 2 shows. The first group is the void path, which has $P_{ie}(t) < 0.03$ at all times. In this group, the conversion of species from i to e is negligible even with a theoretical equation to interpret the reaction. In the second group, the path with $P_{ie}(t) > 0.03$ and the disturbance of $P_{ie}(t) < 0.01$ were defined as stable paths. This definition means that species e was convened from species i without time dependence. In the third group, paths with time-dependent $P_{ie}(t)$ were considered time-variant paths, and most transform paths belong to group 3. Group 2 and group 3 are shown in Figure 2 with different colors.

Table 2. Path Classification

path type	P_{ie} feature
void path	$P_{ie} < 0.03$
stable path	$P_{ie} > 0.01$ and $\Delta P_{ie} < 0.01$
time-variant path	P_{ie} depends on time

Table 3. Symbol Description for eqs 3 to 9

symbol	explanation
C_i	concentration of species i
T	exposed time
I	target species
J	species that can react with i and yield other species
L	species that can yield i in the chemical equations
K	species that can react with l and yield i in the chemical equations
$r_{i,j}$	rate constant for the equation that uses i and j as reactants
R_i	yield rate of species i due to irradiation
ρ	solution density
Ψ	absorbed dose rate
G_i	G value for species i
F	Faraday constant
$Pcc_{l,i}$	PCC value for species l and i
N	length of the data list
V	data serial number in the data list
$V_{ie}(t)$	convention rate from species i to e at time t
E	product species in chemical equations that use i as a reactant
X	possible product species in chemical reactions by species i
$P_{ie}(t)$	convention possibility from species i to e
deg_i^+	species i indegree[a]
deg_i^-	species i outdegree[b]
deg_i	sum of indegree and outdegree for species i

[a]Indegree: the number of product types from the target species by chemical reactions. [b]Outdegree: the number of reactant types that can yield the target species by chemical reactions.

RESULTS

Element Transport Roadmap (ETR). The element transport roadmap (ETR) denotes the efficient element transport paths in the chemical reactions. The ETR was drawn from the analysis of 32 species based on big data on time-scale species concentrations and the corresponding chemical equations. The possible transport paths were provided based on the chemical equations. Then, those paths were classified into three groups according to different P_{ie} features, the stable and time-variant paths were retained, and the void paths were removed. Table 4 and Figure 1 are instances of the calculation of the $ClOH^-$ transport path efficiency by V_{ie} and P_{ie}.

First, all chemical equations that use $ClOH^-$ as a reactant were listed.

Second, V_{ij} for each product was calculated. In Table 4,

$$V_{ClOH^-,Cl^-} = 8 \times 10^9 \times C_H \times C_{ClOH^-} + 10^{10} \times C_{eq^-} \times C_{ClOH^-} + 6.1 \times 10^9 \times C_{ClOH^-}$$

$$V_{ClOH^-,Cl^-} = 9 \times 10^4 \times C_{Cl^-} \times C_{ClOH^-}$$

$$V_{ClOH^-,Cl^-} = 2.1 \times 10^{10} \times C_{H^+} \times C_{ClOH^-}$$

Third, P_{ij} was calculated. In Table 4, the denominator for P_{ij}.is

$$\sum V_{ix}(t) = V_{ClOH^-,Cl^-} + V_{ClOH^-,Cl_2^-} + V_{ClOH^-,Cl^-}$$

Last, P_{ie} for the complete simulation time was plotted and those paths were classified into different groups. The paths from $ClOH^-$ to Cl^- or Cl are time-varying paths, and the path from $ClOH^-$ to Cl_2^- is a void path because of the low $P_{ClOH^-,Cl2^-}$.

Hydrogen, oxygen, and chlorine reactions were analyzed with the corresponding ETRs. In the H ETR, time-variant paths are the overwhelming majority, and these complex time-variant paths display the fixability of the H element transformation network. In the O ETR, species have directional close relationships by effective paths that have high P_{ie}. In the Cl ETR, species have a clear feature with transformation paths, and special species $ClOH^-$ and other Cl formed only species are linked by time-variant paths and the remaining species are linked by stable paths. Oxychloride species use stable paths to contract themselves in the O and Cl ETRs.

Pearson Correlation Coefficient (PCC) Calculation. Figure 3a shows the PCC for all possible special pairs in the chemical reaction induced by electron radiolysis. The species can be classified into different groups according to the PCC value. More details about the classification can be seen in the Discussion section. Species pairs with high correlation were arranged in the same group. Figure 3b1 shows that the high PCC species pair has a similar shape. Meanwhile, the low PCC species pairs have significantly different shapes, as shown in Figure 3b2.

DISCUSSION

Complexity Analysis for Element Transport Roadmap (ETR). The complexity of the ETR is qualified by the number of paths connecting special species in the ETR. The indegree is the number of species that can transform into destined species. The outdegree is the number of destined species transformed from a special species. The degree is the sum of the indegree and outdegree in an ETR. The species degree for the H ETR was calculated from Figure 2a2. It can be seen from the species degrees of H_2O (15) and H_2O_2 (10) that these two species are

https://doi.org/10.1021/acsomega.2c01010
ACS Omega 2022, 7, 15113−15122

Table 4. $ClOH^-$ Transformation Path Efficiency Calculation

equation number	equation	rate constant	product	V_{ie}	P_{ie}
87	$H + ClOH^- = Cl^- + H_2O$	8×10^9	Cl^-	V_{ClOH^-,Cl^-}	P_{ClOH^-,Cl^-}
79	$e_{aq}^- + ClOH^- = Cl^- + OH^-$	1×10^{10}			
113	$ClOH^- = OH + Cl^-$	6.1×10^9			
110	$Cl^- + ClOH^- = Cl_2^- + OH^-$	9×10^4	Cl_2^-	$V_{ClOH^-,Cl2^-}$	$P_{ClOH^-,Cl2^-}$
102	$H^+ + ClOH^- = Cl + H_2O$	2.1×10^{10}	Cl	$V_{ClOH^-,Cl}$	$P_{ClOH^-,Cl}$

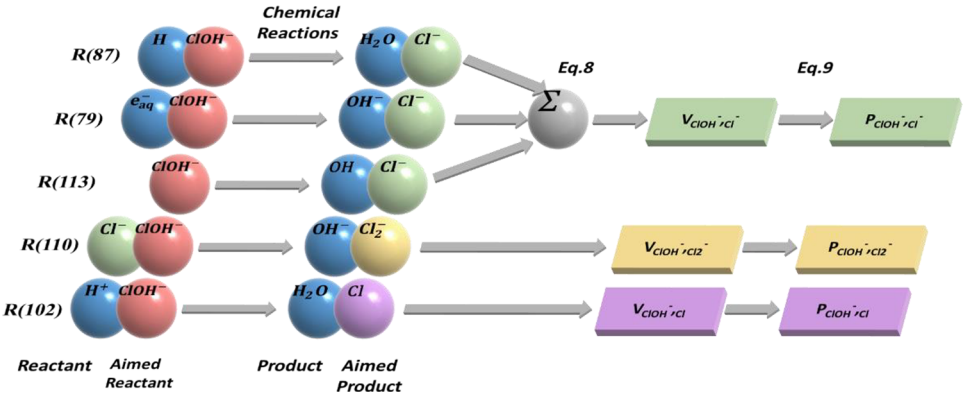

Figure 1. $ClOH^-$ transformation path efficiency calculation in the Cl ETR.

the dominating transformation stations in the H element transport system. This is because H_2O is the original species in solution. Moreover, H_2O_2 has high activity, can be the reactant in bountiful reactions, and is the product of multiple species. The indegree of HO_3 (0) and outdegree of HO_3 (1) means that no species produces HO_3 in the H ETR. However, the $P_{ie}(t)$ of the reaction to produce HO_3 is small, inducing an insignificant transformation path. Therefore, the HO_3 production paths are not shown in Figure 2a2.

The H element transport network is maneuverable, and most species have multiple removal paths. Figure 2a2 shows that H_2O is the core transport station, is the largest source, and saves the most H atoms.

Figure 2b2 is the O ETR. The species degree of OH^- (10) suggests that OH^- is a dominant transport station for the O transport network. The species indegree of O_2 (7) indicates that complex reactions produce O_2. Moreover, species outdegrees of O_2 (2) suggest that O_2 only has two removal paths in the reaction. Thus, bubbles easily form in the solution because the species O_2 generation rate is higher than the destruction rate. The indegree for species O_3 and Cl_2O is zero, meaning that the forming paths for these two species are removed in the O ETR because of low $P_{ie}(t)$.

Species in Figure 2b2 were classified into two groups. The first group includes O_4, Cl_2O_4, ClO_2, ClO_3^-, ClO, ClO_2^-, and Cl_2O_2, and the second group includes the remaining species. Group 1 is mainly formed by oxychloride and O_4. Transformation paths for group 1 species except for ClO_2^- are almost stable. These paths are stable because reactions between group 1 species are sampled, and there are absolute disparities in the concentration of group 1 species. Thus, the effective transformation paths between species of group 1 are few. Group 2 species build a complex and flexible transport network with time-variant transformation paths based on chemical reactions.

Figure 2c2 shows the Cl ETR with all possible transformation paths. Cl_2^- has the largest degree, which suggests that Cl_2^- is an important species. The species indegree of Cl_2O (0) means that the Cl_2O yield paths are too small to be considered. Similar to the previous discussion, we classified the species into two groups: the first group included Cl_2O_4, ClO_2, ClO_3^-, ClO, ClO_2^-, and Cl_2O_2, and the second group included the remaining species. Species transformation paths in group 2 are time-varying. HClO and HCl are the bridge that links the two groups. The first group species can transform to the second group species, but not vice versa.

ETR uses species transformation paths to exhibit the contact for species based on chemical reaction and species concentration data. The dominant species and important species were discovered by ETR. Species were classified into several groups for the Cl ETR and O ETR according to the transformation path features between them, which will simplify the complex species relationship.

PCC Result Analysis Based on the ETR. According to Figure 3a, species were classified into three groups based on the PCC analysis. The PCC of the species pair in the identical group was high. Moreover, the PCC of the species pair in different groups was low. The classification is shown in Table 5.

The PCCs between the species pairs in group I, such as H_2O-Cl^-, H-eh^-, OH^--O^-, and $ClOH^-$-OH are high. This result indicates that correlation bandings are only formed between the special species pairs. In group II and group III, the PCCs between every species in the identical group are high, as shown in Figure 3a. Here, species pairs with PCCs > 0.99 are listed in Table 6.

The relationship between the high PCC species pairs was interpreted by ETR, as shown in Figures 2 and 4. As shown in Figure 2, the transformation paths between species pairs with direct paths are single steps. For instance, the PCC value between O_4 and O_2 is more than 0.99, which can be interpreted as the transformation path between O_4 and O_2 being a single-step reaction, as shown in equation K108 (SI). Moreover, the PCC value between ClO_2 and Cl_2O is also higher than 0.99. However, the single-step reaction between ClO_2 and Cl_2O is absent from the reaction equation list in the

https://doi.org/10.1021/acsomega.2c01010
ACS Omega 2022, 7, 15113−15122

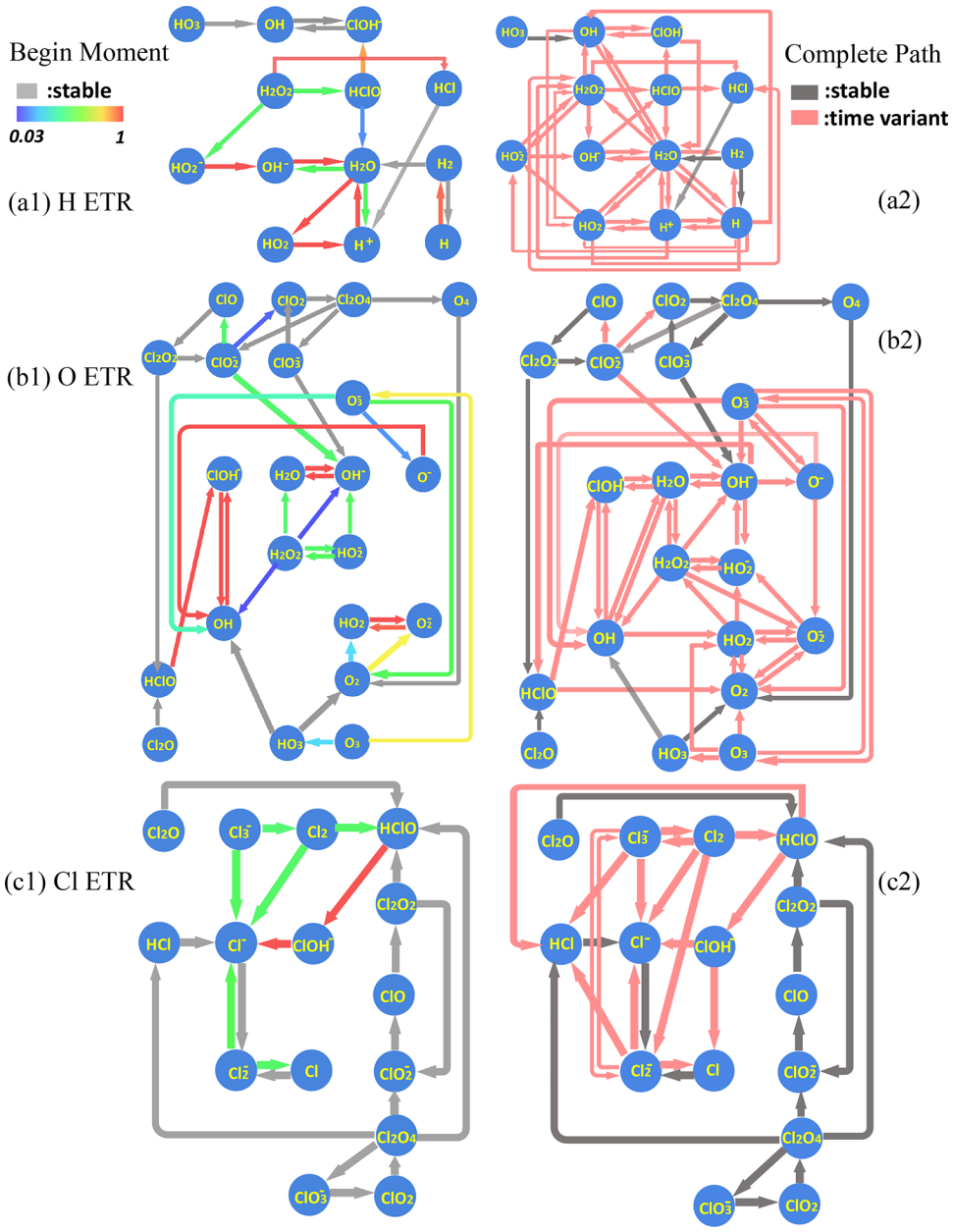

Figure 2. (a1) Initial H ETR (element transport roadmap). (a2) Complete H ETR. (b1) Initial O ETR. (b2) Complete O ETR. (c1) Initial Cl ETR. (c2) Complete Cl ETR. Arrows are transport paths, arrow colors from blue to red represent path transformation percentages from 99 to 3% for time-varying paths, and gray arrows are stable transformation percentage paths.

SI. Only a multiple-step reaction (Cl_2O - HClO - Cl_2O_2 - ClO - ClO_2^- - Cl_2O_4 - ClO_2), as shown in Figure 4a, links the ClO_2-Cl_2O pairs with a high PCC value. In contrast to the species pairs with time-variant paths, as shown in Figure 4b, the transformation paths between the species list in Figure 4a are stable.

The indirect transformation path group species pairs in the ETR lack the direct transformation path. However, species in one pair in the indirect path group both have the same strong linear correlation species. This intermediate species could be the bridge to contact the species pairs and induce high linearity. Figure 4a shows that the species pair of Cl_2O_4 and O_4 is an important bridge that links the Cl ETR to the O ETR. Moreover, these species pairs have a high correlation and stable transformation path. Similar to Cl_2O_4 and O_4, the oxychloride species (ClO, ClO_2^-, ClO_3^-, Cl_2O_2, Cl_2O, ClO_2, Cl_2O_4) are in contact with each other by stable transformation paths. Another species, HCl and oxychloride, showed a strong relationship because of the stable transformation paths from HCl to Cl_2O_4.

No direct stable transformation path or effective intermediate species contacts O_2 and H_2. Thus, instead of the ETR, chemical reactions were analyzed to determine the relationship between O_2 and H_2. The most important reactions of the O_2-H_2 pair were selected according to the reaction rate. Clearly, H_2 is mainly formed by H_2O, which reacts with eh^- or H atoms, and H_2 mainly reacts with OH to consume itself. O_2 is yielded from OH, HO_2, and O_2^-, and O_2 mainly reacts with eh^- or H atoms. Thus, OH, H, and eh^- could be the intermediate species to provide a unique relationship for the O_2-H_2 pair.

https://doi.org/10.1021/acsomega.2c01010
ACS Omega 2022, 7, 15113−15122

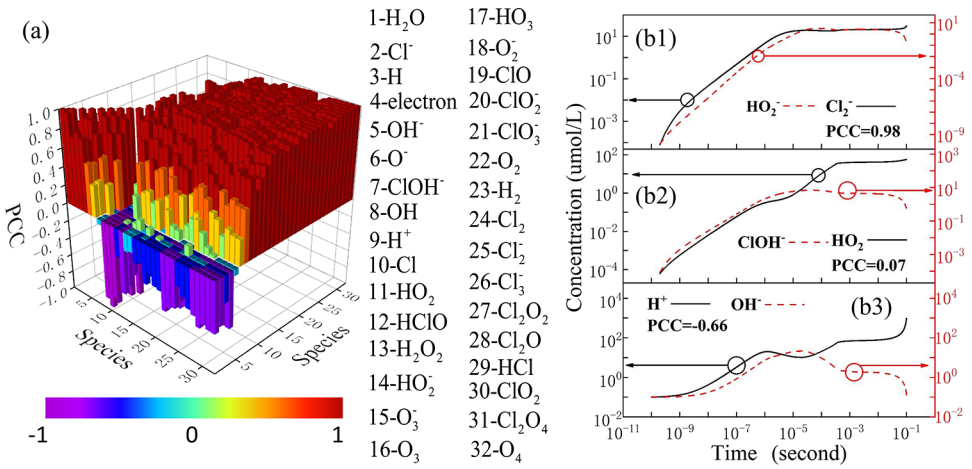

Figure 3. (a) PCC (Pearson correlation coefficient) for each species pair. The *x* axis represents the first species, the *y* axis represents the second species, and the color and height represent the PCC value. (b1). Time-varying Cl_2^- concentration (solid line, left label) and HO_2^- concentration (dotted line, right label). (b2). Time-varying HO_2 concentration (solid line, left label) and $ClOH^-$ concentration (dotted line, right label). (b3). Time-varying H^+ concentration (solid line, left label) and OH^- concentration (dotted line, right label). It is easy to see the relationship between different shapes and PCCs.

Table 5. Species Classification

group	species
I	H_2O↔ Cl^-, H↔ eh^-, OH^-↔ O^-, $ClOH^-$↔ OH
II	H^+, Cl, HO_2
III	HClO, H_2O_2, HO_2^-, O_3, O_3^-, HO_3, O_2^-, ClO, ClO_2^-, ClO_3^-, O_2, H_2, Cl_2, Cl_2^-, Cl_3^-, Cl_2O_2, Cl_2O, HCl, ClO_2, Cl_2O_4, O_4

Table 6. PCC > 0.99 Species Pairs

	indirect path[b]		
direct path[a]	stable path	time-variant path	
O_3^- ↔ O_3	ClO_2 ↔ O_4	Cl_2^- ↔ ClO	O_3 ↔ ClO
O_3 ↔ HO_3	O_2 ↔ HCl	Cl_3^- ↔ HClO	HO_3 ↔ Cl_2^-
O_2 ↔ O_4	HCl ↔ O_4	Cl_3^- ↔ ClO	HO_3 ↔ Cl_2^-
ClO_2 ↔ Cl_2O_4	Cl_2O ↔ O_4	Cl_3^- ↔ ClO_2-	HO_3 ↔ HClO
ClO_2^- ↔ Cl_2O_2	HClO ↔ ClO	Cl_3^- ↔ ClO_3-	HO_3 ↔ ClO
ClO_2 ↔ ClO_3^-	ClO_2 ↔ ClO_2^-	Cl_3^- ↔ Cl_2O_2	O_3^- ↔ HO_3
HCl ↔ Cl_2O_4	ClO_2 ↔ HCl	ClO_2 ↔ Cl_2	O_3^- ↔ ClO
Cl_2O_4 ↔ O_4	ClO_2 ↔ Cl_2O_2	Cl_2 ↔ HCl	O_3 ↔ Cl_3^-
	Cl_2O_2 ↔ Cl_2O	Cl_2 ↔ Cl_2O_2	O_3 ↔ HClO
	ClO_2^- ↔ Cl_2O	Cl_2 ↔ Cl_2O_4	HO_2^- ↔ HO_3
	ClO_3^- ↔ Cl_2O_2	Cl_2 ↔ Cl_2O	H_2 ↔ ClO_2
	ClO_3^- ↔ Cl_2O	Cl_2 ↔ O_4	H_2 ↔ HCl
	ClO_2 ↔ Cl_2O	HO_2^- ↔ O_3^-	H_2 ↔ Cl_2O_4
	Cl_2O_4 ↔ Cl_2O	HO_2^- ↔ O_3	H_2 ↔ O_4
	ClO_2^- ↔ ClO_3^-		

[a]A direct path between species pairs, as shown above, means that the transformation between the species pairs can be completed in one reaction. [b]Species pairs in the indirect path group need multiple reactions to complete the species transformation in ETRs.

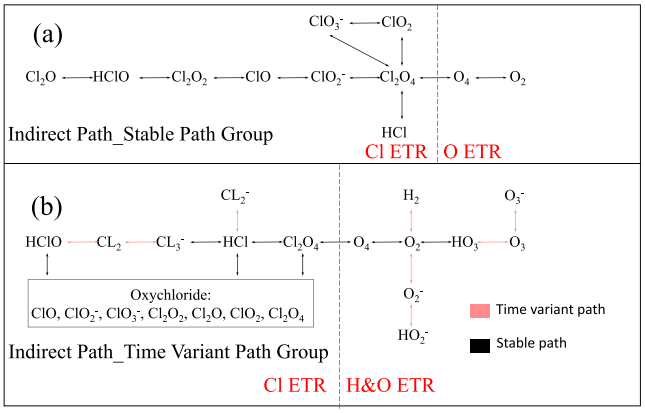

Figure 4. Species transformation network for indirect paths. This figure shows the intermediates for species pairs in the Table 6 indirect path group, which includes stable path parts (a) and time-variant path parts (b).

The relationship between each species was analyzed by PCC calculation, which provided an efficient approach to analyze the radiolysis and reaction by a big data method. However, PCC data are defective in indicating the complete connection for all species because PCC results are not based on the complete transformation paths, as shown in the ETR, but are only calculated by the concentration data of two species. The transformation paths were ignored in the PCC calculation, inducing the low linearity of core species with other species. On the other hand, PCC is based on calculated concentration data that include complete chemical reaction information, although the ETR only analyzes the important reactants and overlooks other reactant influences on the species. Thus, the ETR analysis method can help to identify the dominant species, which is a protagonist in chemical reactions, and PCC is an effective tool for providing highly correlated species pair information that we cannot find in the ETR.

pH, Oversaturated Gas, and the Difference between Saline and Pure Water. Solution pH is well known as a time-varying property during the radiolysis process because chemical reactions change the H^+ concentration. Moreover, when the radiolysis process is sufficiently long, the solution cannot dissolve all the O_2 and H_2 yielded by chemical reactions, and these gases quickly form bubbles and keep the concentrations of O_2 and H_2 constant in the solution.

In Figure 5a1, the pH decreases at a high rate before 10^{-6} s, and then the pH increases. Finally, the pH in a low stage suggests that the solution became acidic. The unusual increase in pH during 10^{-6}–10^{-4} s can be explained in terms of chemical reactions. Several reaction equations that include H^+

https://doi.org/10.1021/acsomega.2c01010
ACS Omega 2022, 7, 15113−15122

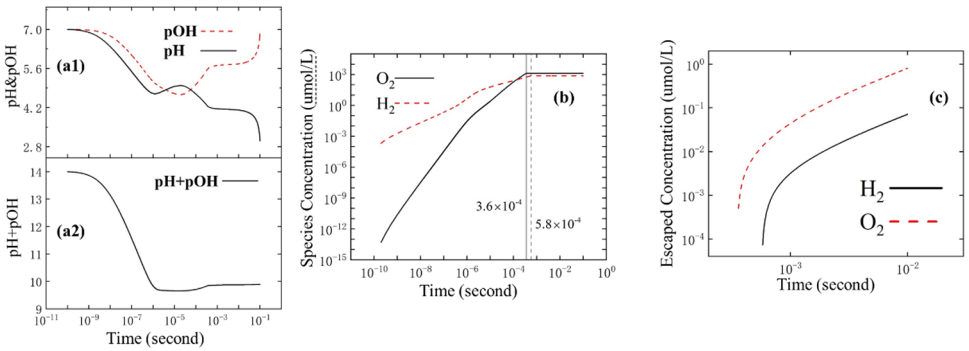

Figure 5. (a1) pH and pOH of solution versus time. pH undergoes a drastic change in 0.1 s. (a2) Time variation of pH + pOH. (b) Time variation of O_2 concentration (solid line) and H_2 concentration (dotted line); the straight line is the gas saturation moment. (c) Escaped concentration for H_2 (solid line) and O_2 (dotted line). O_2 escaped before H_2, but both species have the same curve track.

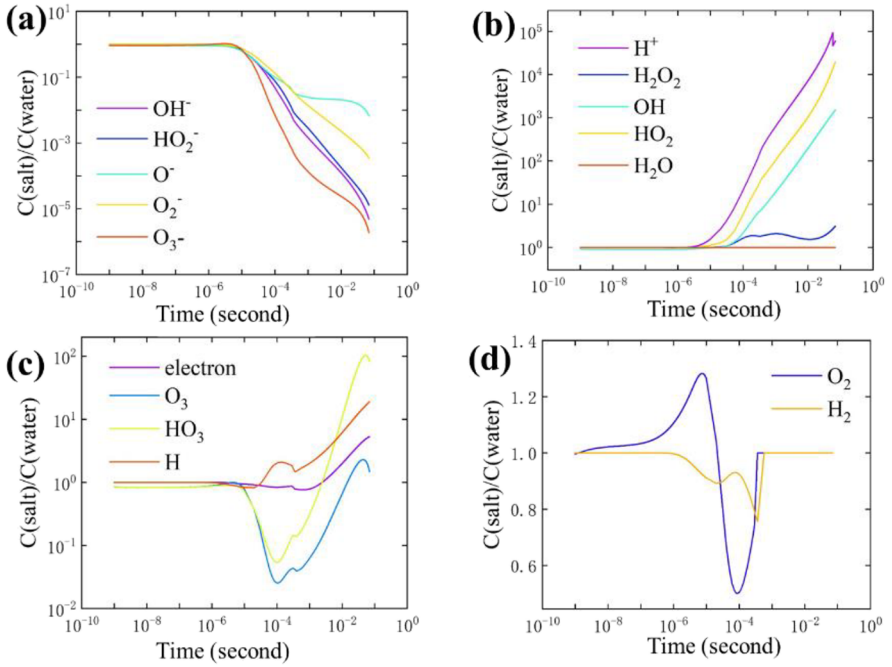

Figure 6. Species concentration ratio between the salt solution and pure water. x axis is time, and y axis is $C_{salt}/C_{purewater}$. (a) Species whose concentrations are lower in salt solution rather than pure water. (b) Species whose concentrations are higher in salt solution rather than pure water. (c) Species whose concentrations are first lower and then higher in salt solution rather than pure water. (d) O_2 and H_2 concentration ratio in salt solution and pure water.

as a reactant or product and with a high reaction rate were analyzed as key equations. The rate of the chemical reaction that yields H^+ always increases, while the H^+ consumption chemical reaction rate increases and decreases. Thus, a possible reason is that the H^+ decrease rate grew faster than the H^+ increase rate and induced an increase in pH. The concentrations of HO_2^- and O_2^- increased, and the two species can react with H^+. Thus, the increase in HO_2^- and O_2^- concentrations accelerated the H^+ consumption rate and finally induced an increase in pH during 10^{-6}–10^{-4} s.

Figure 5c shows that the shape of the escaped O_2 concentration is similar to that of H_2, and the O_2 dissolution saturation time is shorter than that of H_2. However, O_2 is more soluble than H_2 in solution, suggesting that O_2-related reactions are stronger than H_2-related reactions.

To find the differences in radiolysis inference between pure water and saline solution, species concentration databases of pure water and saline solution were plotted against time, as shown in Figure 6.

Here, we only consider those species that appeared in pure water under electron beam exposure.

The Schneider pure water model[26] was used to calculate the species concentration variation in pure water. The G value is identical for the same species in pure water and saline solution, and the saline solution has a G value for Cl^- in addition. Other settings, including the calculation step, the initial value, and the simulation completion time, were identical for the two types of solutions. In Figure 6, the salt–water model species concentrations approach pure water before 10^{-6} s, and then the two models' concentrations become different for most species.

After 10^{-5} s, the concentration ratios differ. Species OH^-, HO_2^-, O^-, O_2^-, and O_3^- are always in the decreasing stage (Figure 6a), which indicates that these species are less abundant in saltwater than in pure water. Moreover, species

https://doi.org/10.1021/acsomega.2c01010
ACS Omega 2022, 7, 15113–15122

H^+, H_2O_2, OH, HO_2, and H_2O are in the opposite state (Figure 6b). The concentration ratios of species eh^-, O_3, HO_3, and H initially decrease and then increase (Figure 6c). O_2 and H_2 have multiple trend changes and finally obtain ratios of 1 (Figure 6d) because both species remain at saturation concentrations.

From Table 7, the yields of OH^-, H_2O_2, HO_2, O^-, O_3^-, O_3, HO_3, and H_2O and the applied rate in pure water are higher

Table 7. Variation Rate of 16 Species in 10^{-3} s by Two Models[a,b]

species	reaction rate (μmol L^{-1} s^{-1})				
	yield by water	yield by salt	applied in water	applied in salt	C_{salt}/C_{water} ratio
eh^-	4.8×10^3	15	2.7×10^7	2.7×10^7	7.8×10^{-1}
H^+	1.1×10^6	5.7×10^7	3.2×10^7	8.9×10^7	6.2×10^2
OH^-	5.2×10^{10}	1.7×10^8	5.2×10^{10}	1.8×10^8	1.5×10^{-3}
H_2O_2	5.2×10^{10}	1.6×10^8	5.2×10^{10}	1.8×10^8	2.0
HO_2^-	5.2×10^{10}	1.5×10^8	5.2×10^{10}	1.5×10^8	2.8×10^{-3}
H	9.6×10^4	1.8×10^6	7.8×10^6	9.6×10^6	2.0
OH	5.0×10^7	2.8×10^{10}	7.6×10^7	2.8×10^{10}	1.9×10^1
O^-	4.0×10^7	1.0×10^6	4.0×10^7	1.1×10^6	2.5×10^{-2}
HO_2	2.5×10^7	7.0×10^7	2.6×10^7	7.1×10^7	1.0×10^2
O_2^-	3.7×10^7	6.3×10^7	3.6×10^7	6.3×10^7	1.4×10^{-2}
O_2	2.2×10^7	2.3×10^7	1.5×10^7	1.5×10^7	1
H_2	2.5×10^3	3.8×10^3	9.4×10^4	1.3×10^6	1
O_3^-	1.9×10^6	4.1×10^4	1.9×10^6	4.2×10^4	1.4×10^{-4}
O_3	2.6×10^5	664	2.6×10^5	666	6.2×10^{-2}
HO_3	963	302	975	302	3.1×10^{-1}
H_2O	5.2×10^{10}	2.0×10^8	5.2×10^{10}	1.5×10^8	1

[a]This table uses the pure water model and salt solution model results to calculate the rate for listed species. Only species that appeared in the two models were considered. This table uses species concentration data at 10^{-3} s. [b]"Yield by water" is the yield speed of species concentrations in the pure water model, and "applied in salt" is the consumption speed of species concentrations in the salt solution model.

than those in salt solution. The yield and applied rate of species H, OH, HO_2, O_2^-, H_2, and H^+ are lower in pure water than in salt solution. O_2 has approximate data for yield and applied rate in the two solutions. The yield rate for eh^- is much better in pure water than in saline solution, and the applied rate is similar in the two solutions.

For species OH^-, HO_2, O^-, O_3^-, O_3, HO_3, and H_2O, their reaction rates are higher in pure water than in saline solution, and the concentrations in pure water are higher than those in salt solution, suggesting that the addition of Cl decreases their reaction rate and provides a negative environment to accumulate these species. In contrast, the saline solution provides a positive environment for the accumulation of species H, OH, HO_2, O_2^-, and H^+ with a high reaction rate. In contrast to other species, the accumulation rate of H_2O_2 species is high in saline solution, but the reaction rate is high in a pure water environment. This is because the difference between the provision rate and depletion rate of H_2O_2 in saline solution is lower than that in pure water. O_2 and H_2 are already oversaturated in both solutions; thus, their concentrations in solution are constant. H_2O has a larger basic concentration, and the yield and consumed concentration can hardly infer the H_2O data. Thus, the H_2O data in the two types of environments are similar.

CONCLUSIONS

In this article, we built the ETR of the chemical reaction induced by high-energy electron radiolysis (HEER) based on the chemical reaction equation and big data analysis. Based on the simulation and PCC analysis, the highly linear species pairs were selected and interpreted by the ETR. The ETR provides essential information on the chemical reaction, such as the element transport, reaction rate, and reaction direction. Combining ETR and PCC analysis, we developed an effective and reliable method for analyzing the complex chemical reaction induced by high-energy electron radiolysis in saline solution. The time variation of pH and bubble formation induced by high-energy electron radiolysis were analyzed based on this method.

ASSOCIATED CONTENT

Supporting Information

The Supporting Information is available free of charge at https://pubs.acs.org/doi/10.1021/acsomega.2c01010.

Complete chemical reactions; electron beam dose rate calculation method; G value calculation method; calculation method contrast; complete PCC data; species concentration in the temporal evolution (PDF)

AUTHOR INFORMATION

Corresponding Authors

Hongxuan Guo − *SEU-FEI Nano-Pico Center, Key Laboratory of MEMS of Ministry of Education, School of Electronic Science and Engineering, Southeast University, Nanjing 210096, People's Republic of China; Center for Advanced Materials and Manufacture, Joint Research Institute of Southeast University and Monash University, Suzhou 215123, People's Republic of China;* orcid.org/0000-0002-8092-8057; Email: ghx@seu.edu.cn

Litao Sun − *SEU-FEI Nano-Pico Center, Key Laboratory of MEMS of Ministry of Education, School of Electronic Science and Engineering, Southeast University, Nanjing 210096, People's Republic of China; Center for Advanced Materials and Manufacture, Joint Research Institute of Southeast University and Monash University, Suzhou 215123, People's Republic of China;* orcid.org/0000-0002-2750-5004; Email: slt@seu.edu.cn

Authors

Zhihao Zhang − *SEU-FEI Nano-Pico Center, Key Laboratory of MEMS of Ministry of Education, School of Electronic Science and Engineering, Southeast University, Nanjing 210096, People's Republic of China*

Bo Liu − *SEU-FEI Nano-Pico Center, Key Laboratory of MEMS of Ministry of Education, School of Electronic Science and Engineering, Southeast University, Nanjing 210096, People's Republic of China*

Dali Xian − *SEU-FEI Nano-Pico Center, Key Laboratory of MEMS of Ministry of Education, School of Electronic Science and Engineering, Southeast University, Nanjing 210096, People's Republic of China*

Xuanxuan Liu − *SEU-FEI Nano-Pico Center, Key Laboratory of MEMS of Ministry of Education, School of Electronic Science and Engineering, Southeast University, Nanjing 210096, People's Republic of China*

https://doi.org/10.1021/acsomega.2c01010
ACS Omega 2022, 7, 15113−15122

Bo Da − *Research and Services Division of Materials Data and Integrated System, National Institute for Materials Science, Ibaraki 305-0044, Japan*

Complete contact information is available at: https://pubs.acs.org/10.1021/acsomega.2c01010

Author Contributions

‖Z.Z. and H.G. contributed equally.

Author Contributions

Z. Z. and H. G. conceived the study, analyzed the data, and wrote the original draft. B. L., D. X., and X. L. took part in the result discussion. B. D. provided the calculation method. All authors gave suggestive feedback. L. S. supervised the entire work.

Notes

The authors declare no competing financial interest.

■ ACKNOWLEDGMENTS

This work was financially supported by the National Natural Science Foundation of China (Grant no. 11874105).

■ REFERENCES

(1) Ren, J.-G.; Xia, H.-L.; Just, T.; Dai, Y.-R. Hydroxyl radical-induced apoptosis in human tumor cells is associated with telomere shortening but not telomerase inhibition and caspase activation. *FEBS Lett.* **2001**, *488*, 123−132.

(2) Valko, M.; Izakovic, M.; Mazur, M.; Rhodes, C. J.; Telser, J. Role of oxygen radicals in DNA damage and cancer incidence. *Mol. Cell. Biochem.* **2004**, *266*, 37−56.

(3) Peckys, D. B.; Mazur, P.; Gould, K. L.; de Jonge, N. Fully Hydrated Yeast Cells Imaged with Electron Microscopy. *Biophys. J.* **2011**, *100*, 2522−2529.

(4) de Jonge, N.; Peckys, D. B. Live Cell Electron Microscopy Is Probably Impossible. *ACS Nano* **2016**, *10*, 9061−9063.

(5) Lloyd, M. M.; Grima, M. A.; Rayner, B. S.; Hadfield, K. A.; Davies, M. J.; Hawkins, C. L. Comparative reactivity of the myeloperoxidase-derived oxidants hypochlorous acid and hypothiocyanous acid with human coronary artery endothelial cells. *Free Radical Biol. Med.* **2013**, *65*, 1352−1362.

(6) Barbouti, A.; Doulias, P. T.; Nousis, L.; Tenopoulou, M.; Galaris, D. DNA damage and apoptosis in hydrogen peroxide-exposed Jurkat cells: bolus addition versus continuous generation of H_2O_2. *Free Radical Biol. Med.* **2002**, *33*, 691−702.

(7) Shao, L.; Li, Q. H.; Wang, J.; Tan, Z. Fragmentation and rapid shortening of telomere in HeLa cells in the early phase of hydroxyl radical-induced apoptosis. *Cancer Biol. Ther.* **2005**, *4*, 336−341.

(8) Xie, J.; Wang, C.; Wang, N.; Zhu, S.; Mei, L.; Zhang, X.; Yong, Y.; Li, L.; Chen, C.; Huang, C.; Gu, Z.; Li, Y.; Zhao, Y. Graphdiyne nanoradioprotector with efficient free radical scavenging ability for mitigating radiation-induced gastrointestinal tract damage. *Biomaterials* **2020**, *244*, 119940.

(9) Ballinger, S. W.; Van Houten, B.; Conklin, C. A.; JIN, G.-F.; Godley, B. F. Hydrogen Peroxide Causes Significant Mitochondrial DNA Damage in Human RPE Cells. *Exp. Eye Res.* **1999**, *68*, 765−772.

(10) Davies, K. J. A. Protein damage and degradation by oxygen radicals I. General aspects. *Biol. Chem.* **1987**, *262*, 9895−9901.

(11) Powers, E. L. The Hydrated electron, the Hydroxyl Radical, and Hydrogen Peroxide in Radiation Damage in Cells. *Isr. J. Chem.* **1972**, *10*, 1199−1211.

(12) Zhang, Y.; Keller, D.; Rossell, M. D.; Erni, R. Formation of Au Nanoparticles in Liquid Cell Transmission Electron Microscopy: From a Systematic Study to Engineered Nanostructures. *Chem. Mater.* **2017**, *29*, 10518−10525.

(13) Donev, E. U.; Hastings, J. T. Electron-Beam-Induced Deposition of Platinum from a Liquid Precursor. *Nano Lett.* **2009**, *9*, 2715−2718.

(14) Ahn, T.-Y.; Hong, S.-P.; Kim, S.-I.; Kim, Y.-W. In situ liquid-cell transmission electron microscopy for direct observation of concentration-dependent growth and dissolution of silver nanoparticles. *RSC Adv.* **2015**, *5*, 82342−82345.

(15) Liao, H. G.; Cui, L.; Whitelam, S.; Zheng, H. Real-time imaging of Pt_3Fe nanorod growth in solution. *Science* **2012**, *336*, 1011−1014.

(16) Winkler, R.; Fowlkes, J. D.; Rack, P. D.; Plank, H. 3D nanoprinting via focused electron beams. *J. Appl. Phys.* **2019**, *125*, 210901.

(17) Tirumala, V. R.; Divan, R.; Ocola, L. E.; Mancini, D. C. Direct-Write E-Beam Patterning of Stimuli-Responsive Hydrogel Nanostructures. *J. Vac. Sci. Technol., B: Microelectron. Process. Phenom.* **2005**, *23*, 3124−3128.

(18) Gupta, T.; Strelcov, E.; Holland, G.; Schumacher, J.; Yang, Y.; Esch, M. B.; Aksyuk, V.; Zeller, P.; Amati, M.; Gregoratti, L.; Kolmakov, A. Electron and X-ray Focused Beam-Induced Cross-Linking in Liquids: Toward Rapid Continuous 3D Nanoprinting and Interfacing using Soft Materials. *ACS Nano* **2020**, *14*, 12982−12992.

(19) Ballav, N.; Schilp, S.; Zharnikov, M. Electron-Beam Chemical Lithography with Aliphatic Self-Assembled Monolayers. *Angew. Chem., Int. Ed.* **2008**, *47*, 1421−1424.

(20) Krsko, P.; Sukhishvili, S.; Mansfield, M.; Clancy, R.; Libera, M. Electron-Beam Surface-Patterned Poly (ethylene glycol) Microhydrogels. *Langmuir* **2003**, *19*, 5618−5625.

(21) Zharnikov, M.; Grunze, M. Modification of thiol-derived self-assembling monolayers by electron and x-ray irradiation: scientific and lithographic aspects. *J. Vac. Sci. Technol., B* **2002**, *20*, 1793−1807.

(22) Fisher, J. S.; Kottke, P. A.; Kim, S.; Fedorov, A. G. Rapid Electron Beam Writing of Topologically Complex 3D Nanostructures Using Liquid Phase Precursor. *Nano Lett.* **2015**, *15*, 8385−8391.

(23) Anderson, A. R.; Hart, E. J. Radiation chemistry of water with pulsed high intensity electron beams. *J. Phys. Chem.* **1962**, *66*, 70−75.

(24) LaVerne, J. A.; Pimblott, S. M. Scavenger and time dependences of radicals and molecular products in the electron radiolysis of water: examination of experiments and models. *J. Phys. Chem.* **1991**, *95*, 3196−3206.

(25) Le Caër, S. Water Radiolysis: Influence of Oxide Surfaces on H2 Production under Ionizing Radiation. *Water.* **2011**, *3*, 235−253.

(26) Schneider, N. M.; Norton, M. M.; Mendel, B. J.; Grogan, J. M.; Ross, F. M.; Bau, H. H. Electron−Water Interactions and Implications for Liquid Cell Electron Microscopy. *J. Phys. Chem. C* **2014**, *118*, 22373−22382.

(27) Anbar, M.; Thomas, J. K. Pulse Radiolysis Studies of Aqueous Sodium Chloride Solutions. *J. Phys. Chem.* **1964**, *68*, 3829−3835.

(28) Kim, K.-J.; Hamill, W. H. Pulse radiolysis of concentrated aqueous solutions of chloride, iodide, and persulfate ions. *J. Phys. Chem.* **1976**, *80*, 2325−2330.

(29) Pucheault, J.; Ferradlnl, C.; Julien, R.; Deysine, A.; Gilles, L.; Moreau, M. Radiolysis of concentration solutions. 1. Pulse and gamma radiolysis studies of direct and indirect effects in LiCl solutions. *J. Phys. Chem.* **1979**, *83*, 330−336.

(30) Kelm, M.; Bohnert, E. Radiation chemical effects in the near field of a final disposal site - I: Radiolytic products formed in concentrated NaCl solutions. *Nucl. Technol.* **2000**, *129*, 119−122.

(31) Kelm, M.; Bohnert, E. Radiation chemical effects in the near field of a final disposal site - II: Simulation of the radiolytic processes in concentrated NaCl solutions. *Nucl. Technol.* **2000**, *129*, 123−130.

(32) Kelm, M.; Metz, V.; Bohnert, E.; Janata, E.; Bube, C. Interaction of hydrogen with radiolysis products in NaCl solution — comparing pulse radiolysis experiments with simulations. *Radiat. Phys. Chem.* **2011**, *80*, 426−434.

(33) Woehl, T. J.; Moser, T.; Evans, J. E.; Ross, F. M. Electron-beam-driven chemical processes during liquid phase transmission electron microscopy. *MRS Bull.* **2020**, *45*, 746−753.

(34) Jinwen, L.; Jun, H.; Zhangquan, P.; Shaojun, D. Nonisothermal Model for the Electric Double Layer under Constant-Charge Condition. *J. Electroanal. Chem.* **2021**, *563*, 115320.

(35) Okada, T.; Ogura, T. Nanoscale imaging of untreated mammalian cells in a medium with low radiation damage using

scanning electron-assisted dielectric microscopy. *Sci. Rep.* **2016**, *6*, 29169.
(36) Inami, W.; Horiba, D.; Kawata, Y. Cell stimulation by focused electron beam of atmospheric SEM. *Ultramicroscopy* **2019**, *206*, 112823.
(37) Liu, Y.; Mu, Y.; Chen, K.; Li, Y.; Guo, J. Daily Activity Feature Selection in Smart Homes Based on Pearson Correlation Coefficient. *Neural Process. Lett.* **2020**, *51*, 1771−1787.

https://doi.org/10.1021/acsomega.2c01010
ACS Omega 2022, 7, 15113−15122